Available online at www.sciencedirect.com

ScienceDirect

Procedia CIRP 85 (2019) 308–313

www.elsevier.com/locate/procedia

2nd CIRP Conference on Composite Material Parts Manufacturing (CIRP-CCMPM 2019)

Evaluation of anomaly detection capabilities using a non-orthogonal camera angle in pulse-phase thermography

Lucas Bretz[a]*, Torben Hinze[a], Benjamin Häfner[a], Gisela Lanza[a]

[a] *wbk Institute of Production Science, Karlsruhe Institute of Technology, 76131, Germany*

* Corresponding author. Tel.: +49 1523 9502567; fax: +49 721 608 45005. *E-mail address:* lucas.bretz@kit.edu

Abstract

Pulse-phase thermography (PPT) is widely used to nondestructively inspect internal defects in fiber reinforced polymers. However, the challenges using PPT for complex shapes is poorly documented in literature. Only small changes in the object distance have been considered.
Complex parts can have significant variations in object distance and thus, in detected radiation. In this contribution, the effect of a non-orthogonal camera angle with respect to a flat sample, leading to varying object distances and an inhomogeneous sound background area in phasegrams, is investigated. Samples with artificial round and square defects of different sizes are positioned under varying angles with respect to the camera, representing geometric properties of complex parts. The construction of the thermographic system and the experimental setup to systematically vary the angle between camera and specimen is presented. We investigated the change of the signal-to-noise ratio (SNR) of artificial delaminations in PPT measurements under varying object distances. The SNR in a distance of 136 mm out of the focal plane is sufficiently high for image feature extraction. Phasegrams are exported to a colored representation, leading to a higher contrast in distinct color channels. An algorithm which extracts and merges defect information from three different color channels is developed. Challenging lighting conditions lead to a noisy background having artifacts. The developed filter performs better in defect detection and size quantification than a global or local threshold in grayscale phasegrams under those conditions.

Keywords: Analysis, Fiber reinforced plastic, Quality assurance, Thermal effects

1. Introduction

Lightweight components are addressed as one possibility to reduce the overall CO2 emissions [1]. Fiber-reinforced polymers (FRP) have the potential to significantly reduce weight while simultaneously offering high mechanical properties, such as a high stiffness. New hybrid material classes are developed, like continuous-discontinuous fiber reinforced polymers. Sheet Molding Compound (SMC), offering a high design freedom, serves as a discontinuous base material in the hybrid part and is the material of focus in this study. Although FRP have been produced for many years, there are still defects that occur during its production [2]. Material flaws, occurring during the production process, need to be detected for a quality assessment. An inline quality assurance is a potential cost saver compared to an end-of-line control, because the material flaw is detected directly at its origin instead of passing through the whole production process. This work concentrates on the automated detection of artificially created defects resembling foreign bodies and delaminations via thermography. The claim of the defect detection is to operate on complex geometries, featuring inclined slopes, leading to varying object distances out of the focal plane. In this work, the thermographic camera is in a fixed position which leads to economic benefits compared to other methods such as a robotic geometry tracking, as introduced in [3]. The performance of the defect detection is tested using a measurement setup in which slope angles can be varied systematically, allowing to investigate different incrementally changing object distances.

10.1016/j.procir.2019.09.032

2. State of the Art

It is distinguished between active and passive thermography. In active thermography, the inspected part is externally stimulated to investigate the thermal response to the stimulus. The infrared emission response is recorded by an infrared camera. Active thermography proves to be successful in non-destructive testing (NDT) of composite materials [2, 4]. Pulsed phase thermography (PPT) was developed in 1996 and combines the advantages of pulse thermography and modulated thermography (time and phase images) [5]. A transformation algorithm, e.g. the discrete Fourier transform (DFT), is applied to the time series of infrared images representing the temperature evolution on the specimen's surface after the thermal stimulus. The frequency components are determined according to Eq. (1):

$$F(f)=\sum_{k=0}^{N-1}T(k)e^{i\frac{2n\pi kf}{N}}=\mathrm{Re}(f)+i\,\mathrm{Im}(f) \tag{1}$$

F is the Fourier transform, f the frequency, N the number of thermal images k in a sequence, $T(k)$ the temperature at a pixel (u,v) and n the frequency increment. From the DFT, ampligrams $A(f)$ and phasegrams $\Phi(f)$ are accessible. [6] Ampligrams and phasegrams can be calculated by

$$\begin{aligned} A(f)&=\sqrt{\mathrm{Re}^2(f)+\mathrm{Im}^2(f)}\\ \Phi(f)&=\arctan\left(\frac{\mathrm{Im}(f)}{\mathrm{Re}(f)}\right)\end{aligned} \tag{2}$$

Non-uniform heating, variations in surface emissivity and reflections from the environment have a neglectable impact on phase [7]. Additionally, phase responds more sensitively to material thermal properties than to geometrical features and has deeper probing capabilities than amplitude. But it is more affected by noise. [6]

However, literature investigating the NDT application of thermography on FRP mostly deals with planar specimens, not taking more complex geometries into consideration. Ibarra-Castanedo et al. investigated specimens with a curved geometry and inclined slopes of 30° [8]. The implemented Teflon insertions are identified in thermo- and phasegrams. However, the maximum height difference in these test geometries is 60 mm. Pastuszak et al. investigated cylindrical specimens with a radius of 92 mm and positioned a Teflon layer (60 mm x 60 mm) between the plies [9]. The curvature results in a height difference of less than 50 mm. Mayr et al. suggest a viewing angle of less than 60° because of a reduced emissivity ε depending on the viewing angle [10]. Therefore, no reliable infrared measurements are possible beyond this angle. A robot-guided thermographic system is suggested for large 3D parts in the aerospace industry [3].

No study has so far extensively investigated the effects of a non-orthogonal camera angle on the potential of anomaly detection, such as artificially inserted delaminations in SMC.

3. Experimental setup

3.1. Specimens

Two plates have been produced for the examination. The plates consist of a structural SMC based on an unsaturated polyester polyurethane hybrid (UPPH) resin. The fiber volume content of the used material is 23 vol% (41 wt%). One specimen consists of 4 stacked layers of SMC in a B-stage. 15 artificial squared defects and 22 round defects, made out of aluminum and Teflon (PTFE), are integrated between the individual layers. The thickness of the integrated defects is 130 µm (Teflon) and 11 µm (aluminum). The side length of the inserted square defects is 10 mm (equivalent diameter D_{eq} of 11.3 mm according to $D_{eq} = 2L/\pi^{1/2}$), the diameter of the circular defects is 5.5 mm. The same defect geometries have been placed between the first and second layer and between the second and third layer. This results in a defect depth of 0.5 and 1 mm respectively. A depth of 1.5 mm can be investigated by flipping the plate. The initial dimensions are given in Fig. 1.

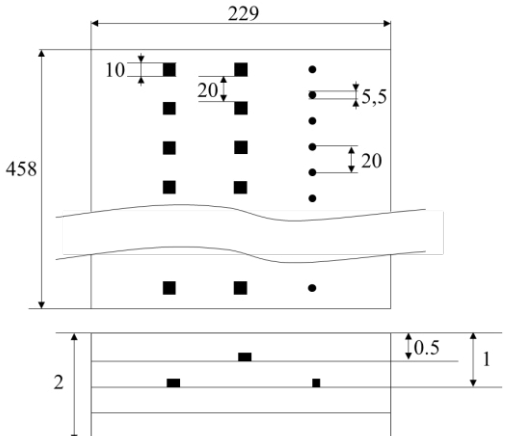

Fig. 1. Technical specification of the specimen

The mold has been heated to 145 °C and closed with a hydraulic press by Lauffer with a maximum press force of 50 kN. Positional deviations of squared and round defects and deformations of the squared defects occurred during the molding process. Therefore, the actual defect size deviates and has been remeasured.

3.2. Apparatus and methods

The designed plate holder is carried by a CNC portal and allows to variate the angle of the specimen compared to the camera plane, illustrated in Fig. 2 (a). The inclination axis of the plate cuts the main axis and the focal plane of the camera. This allows a setup in which the sharp area is always in the center of the image, regardless of the used inclination angle. The edges of the plate move further out of the focal plane when the plate is tilted. The image becomes blurred at its edges.

The thermal stimulation is carried out by a photographic flash, model VH3-6000 by HENSEL-VISIT. The power of the lamp is 6000 J. The image is generated by the thermal imaging camera ImageIR 5300 by InfraTec. The temperature evaluation of the specimen is observed for 60 s after the flash, resulting in a minimal frequency of 0.017 Hz after the DFT. The camera

resolution is 320 x 246 pixels. The objective has a focal length of 25 mm, the object distance is 30 cm. In this setup, the sharp area contains all planes, which are located between +/- 6 mm from the focal point. Post processing, by means of Fourier transform and image selection, is performed with the software DisplayIMG 6 by edevis. Ampli- and phasegrams are exported either as a grayscale or as a color image. The gray values are mapped to the RGB color channels using the color map 'Rain', shown in Fig. 2 (b), for a colored representation. The upper and lower limit of the gray and color scale is determined by the 0.5 percentile of the data. Final image analysis is done using MATLAB.

A checkerboard pattern and the MATLAB routine for camera calibration is used. All inclination angles from 0 - 65° are examined in 5° steps. A measurement is made at each angle and a corresponding calibration image is taken.

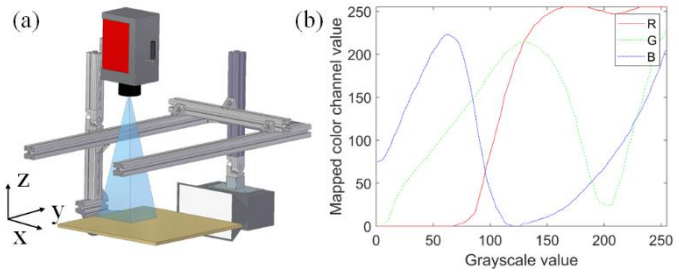

Fig. 2. **(a)** Measurement setup with specimen in horizontal alignment **(b)** Colormap 'Rain' in DisplayIMG6

4. Approach

The following approach is structured in three subchapters. Initially, the signal-to-noise ratio (SNR) is evaluated for the most challenging setup, with a maximum distance of 136 mm out of the focal plane of the camera. Phasegrams are analyzed quantitatively for the algorithm design. Finally, the procedure of feature extraction is described.

4.1. Investigation of Signal-to-Noise-Ratio on inclined slopes

First, the SNR is evaluated in a thermographic grayscale image, directly exported from DisplayIMG 6. The following definition of the SNR is used [11, 12]:

$$SNR = \frac{|\mu_S - \mu_N|}{\sigma_N} \quad (2)$$

Fig. 3. (a) shows the phasegram of the specimen with Teflon squares in 0.5 mm depth (T_S1_sq). The specimen is tilted by 65° around the negative x-axis compared to its horizontal alignment shown in Fig. 2 (a), leading to the most challenging setup. The sharpest region, representing the focal plane, is in the area of defect no. 7. Defect no. 12 is 136 mm out of the focal plane. The manually selected red and blue boxes illustrate the regions which are taken into consideration for the calculation of the SNR. A manual evaluation was conducted because of the difficulty of an automated SNR evaluation and the sensitivity in the choice of reasonable image reasons for signal and noise [11]. The pixel's gray value in the blue box are used for the calculation of the signal's average μ_S. Corresponding, the pixel's gray values in the red box contribute to the noise's average and standard deviation μ_S and σ_N. The SNR for the shown defects is given in Fig. 3 (b). The increased SNR of the detected defects in the blurred regions compared to defect no. 7 can be explained with a smoothed noise, resulting in a decreased standard deviation (cf. Eq. (2)). Thus, an image anomaly detection seems to be a reasonable approach to quantitatively locate defects on inclined composite slopes. The drop in SNR for defect no. 2 is due to illumination conditions and the proximity to the specimen's edge.

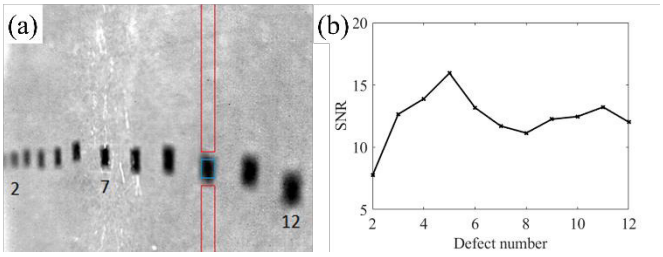

Fig. 3. **(a)** Grayscale phasegram of T_S1_sq_65° with numbered defects **(b)** SNR of defects with different object distance

4.2. Qualitative comparison of color phasegrams at different frequencies

The phasegrams of two different frequencies from the same measurement have been exported in the RGB color space and are illustrated in Fig. 4. Deeper defects appear in the phasegram at lower frequencies, as already explained in [8]. Additionally, defect outlines at both defect depth are not as sharp as in the image with higher frequency. Three effects lead to the fuzzier outlines. First, deeper frequencies extract information from deeper areas. Thus the heat diffusion is stronger. Second, the optimal frequency is not reached for either depth. Third, the appearance of the higher defect reduces the contrast of the color bar in the region of the deeper defect. At the higher frequency, the full color spectrum is used to visualize the defects at the same depth which leads to geometric more precise outlines (squares). At the lower frequency, shapes tend to be round.

In this work, we focus on the detection of defects in the same depth and will not simultaneously evaluate defects at different

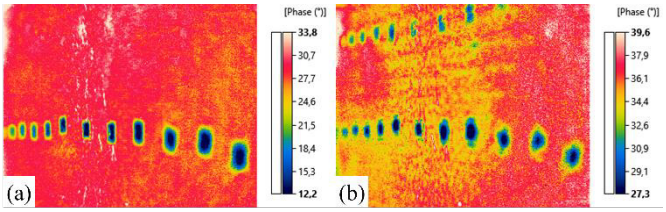

Fig. 4. **(a)** Phasegram of T_S1_sq_65° at 0.117 Hz **(b)** Phasegram of T_S1_sq _65°at 0.033 Hz

depth.

4.3. Data fusion of separate color channel information

Phase shifts of the sound background area occur occasionally in varying manifestations. Light phase shifts can be observed in Fig. 4. (a) out of the focal plane at the higher

frequency. The phase shifts of the sound background are more pronounced at the lower frequency (Fig. 4. (b)). Stronger background phase shifts can occur, as exemplarily illustrated in Fig. 6. A phasegram of specimen A_S1_sq_55° (aluminum defects, 0.5 and 1 mm defect depth, squared defects, inclination angle 55°) with challenging background information is given. The exported color image is separated into its three channels red, green and blue (cf. Fig. 6. (d), (e) and (f)) and compared to its direct grayscale export and a converted grayscale image using the MATLAB function rgb2gray().

The sound background area, which is exemplarily depicted in red, yellow and green in the color image, is exemplarily compared to the pixel values of four defects (no. 5, 6, 8 and 10). The absolute difference between the mean defect and mean background pixel value (contrast) is more pronounced in two out of three color channels compared to the grayscale phasegram. Additionally, a contrast-enhanced grayscale image (lower and upper 20% of gray values are mapped to 0 and 255) still shows a lower contrast than the most pronounced color channel. The doubled mapping (gray to RGB to gray) can reduce the contrast due to compression of the color scale. Results are given in Table 1.

Table 1. Grayscale pixel values compared to color channel pixel values

Image	Mean background px. value around the defects no. 5, 6, 8 and 10	Mean. defect px. value at the defects no. 5, 6, 8 and 10	Absolute diff. between mean defect and background px. value
Gray	192/158/133/121	073/058/024/026	119/100/109/095
Gray-enh.	233/179/137/117	037/016/007/018	196/163/130/106
RGB2Gray	116/180/187/178	101/087/041/043	015/093/146/135
R	252/252/217/187	010/003/003/009	242/243/214/178
G	057/175/206/208	132/108/046/047	075/069/160/161
B	060/018/007/004	182/202/120/109	122/184/112/105

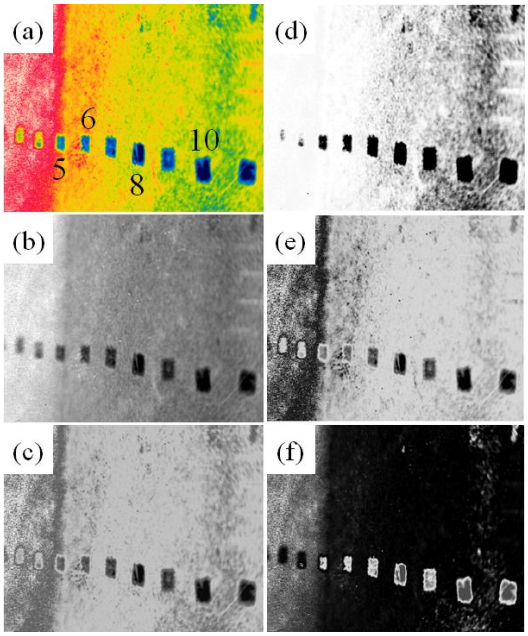

Fig. 6. **(a)** Phasegram of A_S1_sq_55° at 0.2 Hz (**b**) Grayscale phasegram exported from DisplayIMG6 **(c)** Grayscale phasegram RGB2Gray **(d)** R color channel **(e)** G color channel **(f)** B color channel

An evaluation routine is developed which extracts the features of every color channel individually, because of the increased contrast difference in the individual color channels. Initially, a global binary threshold is determined for every color channel according to Otsu's method. This threshold is weighted with the empirically determined factor 0.3 to improve the probability of detection in the first step. Then, the resulting binary filter masks of every color channel are combined (logical disjunction). Regions smaller than 20 pixels are discarded to reduce artefacts. Tests have shown that the threshold of 20 pixels produces the most reliable results. A dynamic region of interest (ROI) in the form of a bounding box is defined around every merged feature, representing a possible defect zone. The bounding box is defined to be 10 % larger than the extracted feature to account for edge effects and ensure proper detection in the fourth step using a local threshold. This local ROI-threshold is determined for the initially detected, potential defect area according to Otsu's method for every color channel and defect. An empirically determined weight factor of 0.7 for the threshold delivered the best results for isolating the defects from the background. In a fifth step, the largest connected area in a ROI, determined by a Blob analysis, is considered as the defect in a specific color channel. The individual features of the color channels are merged (logical conjunction) if the feature also occurs in at least one other color channel to avoid overdetection. The result is a binary filter mask with a black background and defects in white.

The extrinsic and intrinsic camera parameters are determined using the images of a checkerboard calibration pattern. The world coordinates are calculated for the smallest bounding box's corners of a defect to determine its size. This step is consequently performed for each defect zone separately.

The presented algorithm is implemented in MATLAB and its workflow is given in Fig. 5.

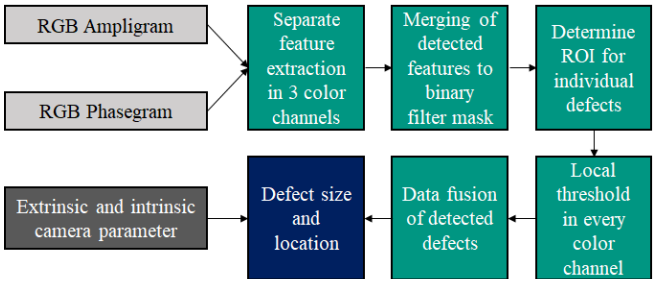

Fig. 5. Workflow of the developed RGB-filter algorithm

5. Results

5.1. Comparison of RGB-filter algorithm to grayscale global and local thresholding

The performance of the developed algorithm is tested against two other methods on a phasegram with changing background. First, the exported grayscale image serves as an input for a local thresholding in a single channel according to the presented algorithm. Second, a classical binary threshold is calculated with Otsu's method. The same phasegrams as given in Fig. 6 (a) and (b) are considered for the evaluation presented in Fig. 7. The RGB-filter algorithm correctly identifies the

delaminations no. 5 to 11, but fails to detect the two delamination on the left edge (no. 3 and no. 4). Those defects have a lower SNR (6.4 and 7) compared to the detected defects (SNR: 8 to 12.5). The same local thresholding method from the RGB-filter applied to the single channel of the grayscale image leads to less detected defects, but improves compared to a global threshold (cf. Fig. 7 (b) and (c)).

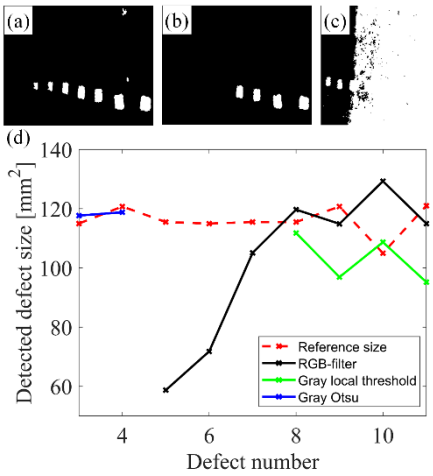

Fig. 7. **(a)** RGB-filter **(b)** Local thresholding on grayscale export from DisplayIMG 6 **(c)** Global Threshold on grayscale according to Otsu **(d)** Comparison of detected defect size

Though, global thresholding of grayscale phasegrams outperforms the RGB-filter for mostly homogeneous background areas, such as exemplarily given in Fig. 4 (a). All defects are detected in the grayscale image of T_S1_sq_65° (μ=89.5 mm², SD = 10.2 mm²), whereas defect no. 2 remains undetected with the RGB-filter (μ= 57.2 mm², SD=15.9 mm²).

However, the RGB-filter proves to be useful due to the processing of the contrast-enhanced image, as phasegrams of inclined slopes tend to have inhomogeneous phase shifts in the sound background areas.

5.2. Testing at incrementally changed inclination angle for squared defects

Furthermore, the algorithm is tested at incrementally changed inclination angles from 0° to 65° in 5° steps for squared defects. Exemplary phasegrams of T_S1_sq are given in Fig. 8.

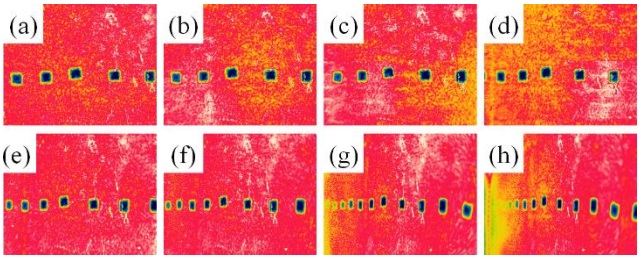

Fig. 8. Phasegrams of T_S1_sq at 0.117 Hz at **(a)** 0° **(b)** 10° **(c)** 20° **(d)** 30° **(e)** 40° **(f)** 50° **(g)** 60° **(h)** 65°

The very left defect in the first image is defect no. 6 and the very right defect no. 10. The center defect is defect no. 8 and remains in the focal plane during the whole measurement series.

The sizes of the detected representations of these defects are evaluated for every angle increment. The result is given in Fig. 9. The defects no. 6 and no. 10 are -/+ 54 mm out of the focal plane in the final position (65°). The mean detected size is 34% smaller than the mean reference size. The average and the standard deviation (SD) of the same detected defect at 14 different inclination angles is given in Table 2. Measurements at individual angles are not repeated.

Flipping the specimen allows to investigate the inserted Teflon defects in the middle (depth 1 mm) as they become the upper defects in this setup. The detected defects' size is 91.3 mm² in average (SD: 18.9 mm²) for defects no. 9 and 10 over all inclination angles. The reference size is 104.5 mm² and 115.5 mm², respectively.

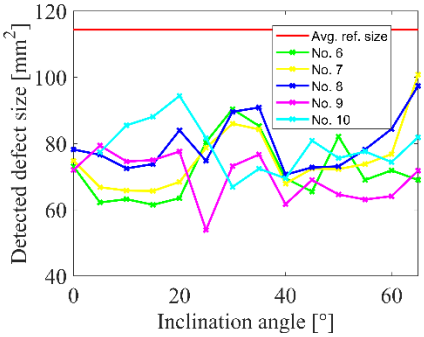

Fig. 9. Detected defect sizes under varying inclination angle for T_S1_sq

Aluminum defects in the depth of 0.5 mm are detected over all angles with an average size of 98.3 mm² (SD: 32.9 mm²) for an average reference size of 116.5 mm² (SD: 2.2 mm²). The defects in the depth of 1 mm are detected with an average size of 98.4 mm² (SD: 20.8 mm²). The detection fails at the maximum angle of 65°. The average measured reference size is 113.3 mm² (SD: 4.4 mm²).

Table 2. Detected avg. defect sizes and standard deviations (T_S1_sq)

Defect no.	Average detected size [mm²]	Standard deviation [mm²]	Underestimation compared to true size [%]
6	71.9	8.9	34.7
7	75.3	9.4	31.5
8	79.8	7.9	27.5
9	69.8	7.0	33.2
10	78.9	7.3	31.6

5.3. Testing at incrementally changed inclination angle for round defects

The implemented round defects represent a significant more challenging detection task because of the smaller area. Only the round Teflon defects at 0.5 mm depth are detected under all inclination angles. The average detected size is 44.3 mm² (SD: 12.3 mm²) for the defects no. 3 to 9 and all inclination angles. The RGB-filter could not identify the round aluminum defects at 0.5 mm depth under all circumstances because of

thresholding problems, depicted in Fig. 10. (a) and (b). Large background artefacts in the sound area influence the determination of an appropriate global threshold for the initial feature extraction in the three color channels. Measurements for all defects no. 4 to no. 10 are obtained at the angles 0°, 5° and from 45° to 65°. An average size of 34.1 mm² (SD: 5.2 mm²) is determined. Fig. 10 (c) illustrates the phasegram for round aluminum defects in 1 mm depth. The algorithm fails in most cases due to thresholding problems in the first step.

Overall, the smaller defects are overestimated in size. The lower influence of a smaller defect on heat conduction is an explanation. The phase difference in Fig. 10. (a) between maximum (red, 25.0) and minimum (blue, 12.3) is smaller compared to exemplarily Fig. 4. (a). Thus, less sharp edges occur in the case of smaller defects. Higher percentage deviations compared to squared defects can further be explained by the higher relative influence of a falsely detected pixel.

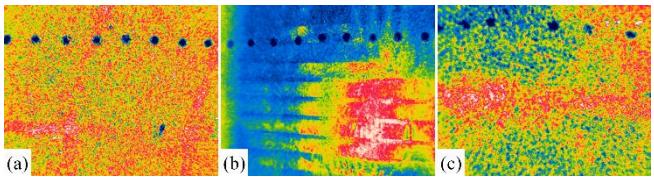

Fig. 10. **(a)** Phasegram of A_S1_r_0° at 0.5 Hz, defects detected **(b)** Phasegram of A_S1_r_30° at 0.5 Hz, defects not detected **(c)** Phasegram of A_S1_r_0°, 0.5 Hz, defects not detected

6. Conclusion and outlook

It is shown that the SNR is sufficiently high when a specimen is moved 136 mm out of the focal plane for the used camera setup. The distance is 23 times larger than the manufacturer's specified sharp area in the region of the focal plane. A workflow to automatically evaluate the thermographic anomaly size of artificial delaminations in SMC is presented. Experimental tests are conducted to assess the performance of the RGB-filter compared to a global and local threshold filter. The benefits of the developed algorithm come into effect under poor image quality through noisy background information and poor illumination conditions. It has been shown that an evaluation of the three contrast-enhanced RGB color channel provides a better detection result than the evaluation of the grayscale image.

The presented RGB-filter detects more anomalies in challenging backgrounds. It allows the automated detection of Teflon and aluminum anomalies of a size of 100 mm². Nevertheless, the algorithm tends to underestimate the reference size for the larger, squared defects. The smaller and round defects (area of 24 mm²) cannot reliably be detected in all cases. It overestimates the size by up to 85% in this case.

Future developments of the algorithm focus on a partial filter mask iterating in a first step through the different color channels. This procedure ensures that already the first anomaly guess is based on a local threshold. It is expected that influences of background artefacts, as depicted in Fig. 10, can be reduced which allows an automated detection of smaller and deeper defects. Additionally, an iteration of the algorithm through a set of frequencies is reasonable to obtain defect information at different depth and chose the proper frequency for image processing individually for every detected defect.

Acknowledgement

The research documented in this manuscript has been funded by the German Research Foundation (DFG) within the International Research Training Group 'Integrated engineering of continuous-discontinuous long fiber reinforced polymer structures' (GRK 2078). The support by the German Research Foundation (DFG) is gratefully acknowledged.

Author Contributions

Lucas Bretz developed the main idea of the application of the automated anomaly detection in thermographic images on inclined composite slopes and initiated the bachelor thesis of Torben Hinze. Lucas Bretz and Torben Hinze developed the algorithm. Torben Hinze performed the major part of the work in terms of thermographic measurements. Benjamin Häfner supported the development and the discussion of the evaluation procedure of the thermographic measurements. He thoroughly revised the paper. Gisela Lanza initiated the research subject and supervised the method development.

References

[1] Europaparlament und Europarat. Zur Festsetzung von Emissionsnormen für neue Personenkraftwagen im Rahmen des Gesamtkonzepts der Gemeinschaft zur Verringerung der CO2-Emissionen von Personenkraftwagen und leichten Nutzfahrzeugen. Verordnung (EG) Nr. 443/2009. Brüssel; 2009

[2] Zaiß M, Jank M-H, Netzelmann U, Waschkies T, Rabe U, Herrmann H-G, Thompson M, Lanza G. Use of Thermography and Ultrasound for the Quality Control of SMC Lightweight Material Reinforced by Carbon Fiber Tapes. Procedia CIRP 2017; 62:33-38.

[3] Schmidt T, Dutta S. Automation in Production Integrated NDT Using Thermography. 4th International Symposium on NDT in Aerospace 2012

[4] Vaara P, Leinonen J. Technology Survey on NDT of Carbon-fiber Composites. Publications of Kemi-Tornio University of Applied Sciences Serie B. Reports 8/2012

[5] Maldague X, Marinetti S. Pulse phase infrared thermography. Journal of Applied Physics 1996; 79:2694-2698.

[6] Ibarra-Castanedo C, Maldague X. Pulsed phase thermography reviewed. Quantitative InfraRed Thermography Journal 2004; 1:47–70.

[7] Busse G, d. Wu, Karpen W. Thermal wave imaging with phase sensitive modulated thermography. Journal of Applied Physics 1992; 8:3962–3965.

[8] Ibarra-Castanedo C, Avdelidis NP, Grinzato EG, Bison PG, Marinetti S, Chen L, Genest M, Maldague X. Quantitative inspection of non-planar composite specimens by pulsed phase thermography. Quantitative InfraRed Thermography Journal 2006; 3:25–40.

[9] Pastuszak PD. Characterization of Defects in Curved Composite Structures Using Active Infrared Thermography. Procedia Engineering 2016; 157:325–332.

[10] Mayr G, Hendorfer G. Characterization of defects in curved carbon fiber reinforced plastics using pulsed thermography. Quantitative InfraRed Thermography Journal 2010; 7:3–16.

[11] Usamentiaga R, Ibarra-Castanedo C, Maldague X . More than Fifty Shades of Grey: Quantitative Characterization of Defects and Interpretation Using SNR and CNR. J Nondestruct Eval 2018 (2): 37

[12] Welvaert M, Rosseel Y. On the definition of signal-to-noise ratio and contrast-to-noise ratio for FMRI data. PLoS ONE 2013: 8(11)